International Journal of Automotive Technology, Vol. 18, No. 4, pp. 707−718 (2017)
DOI 10.1007/s12239−017−0070−0

pISSN 1229−9138/ eISSN 1976−3832

NOVEL ELECTRONIC BRAKING SYSTEM DESIGN FOR EVS BASED ON CONSTRAINED NONLINEAR HIERARCHICAL CONTROL

Ronghui Zhang[1, 2], Kening Li[3)*], Fan Yu[3)], Zhaocheng He[1, 2)] and Zhi Yu[1, 2)]

[1)]Research Center of Intelligent Transportation System, School of Engineering, Sun Yat-sen University, Guangdong 510275, China
[2)]Guangdong Key Laboratory of Intelligent Transportation Systems, Guangdong 510275, China
[3)]State Key Laboratory of Mechanical System and Vibration, School of Mechanical Engineering, Shanghai JiaoTong University, Shanghai 200240, China

(Received 4 July 2016; Revised 18 October 2016; Accepted 22 December 2016)

ABSTRACT−Both environment protection and energy saving have attracted more and more attention in the electric vehicles (EVs) field. In fact, regarding control performance, electric motor has more advantages over conventional internal combustion engine. To decouple the interaction force between vehicle and various coordinating and integrating active control subsystems and estimate the real-time friction force for Advanced Emergency Braking System (AEBS), this paper's primary intention is uniform distribution of longitudinal tire-road friction force and control strategy for a Novel Anti-lock Braking System (Nov-ABS) which is designed to estimate and track not only any tire-road friction force, but the maximum tire-road friction force, based on the Anti-Lock Braking System (ABS). The longitudinal tire-road friction force is computed through real-time measurement of breaking force and angular acceleration of wheels. The Magic Formula Tire Model can be expressed by the reference model. The evolution of the tire-road friction is described by the constrained active-set SQP algorithm with regard to wheel slip, and as a result, it is feasible to identify the key parameters of the Magic Formula Tire Model. Accordingly, Inverse Quadratic Interpolation method is a proper way to estimate the desired wheel slip in regards to the reference of tire-road friction force from the top layer. Then, this paper adapts the Nonlinear Sliding Mode Control method to construct proposed Nov-ABS. According to the simulation results, the objective control strategy turns out to be feasible and satisfactory.

KEY WORDS : Electric vehicle, Constrained active-set SQP algorithm, Parameters identification, Nonlinear sliding mode control, Hierarchical Control

1. INTRODUCTION

As the developments of economy and technology, automobile industry has brought human being much convenience. Car ownership is booming, especially in developing areas. But, the emission and energy shortage problems have become increasingly severe because the cars with internal combustion engines are dominant. Therefore, electrifying vehicles appears to be a solution to the above problems. Environmental protection and energy conservation have attracted more and more researchers' eyes, in recent years. The main benefits of electric vehicles, commercially, are the energy saving and cost competitive advantages. In addition, EVs are actually a typical mechatronic system just like precision machines controlled by computers, robots and so on, because EVs using one or more electric motors for propulsion rather than internal combustion engines. Mechatronics technology, especially the mechatronic control, is developing rapidly and prompting the development of electric vehicles. Several outstanding researches have been working on this aspect of EVs (Attia *et al.*, 2014; Hori, 2004; Kim *et al*., 2015a; Kim and Huh, 2016; Zhang *et al*., 2013a; Noceda and Wright, 2006). Compared with conventional vehicles, EVs, with advanced mechatronic technologies, have safer feature of better driving performance as well as being cleaner and saving energy. Compared with internal combustion engines and hydraulic braking systems, the advanced electric motors have the following most significant advantages: First, they have 10 ~ 100 times faster torque response, bringing them to the millisecond-level; second, there is extremely precise feedback of the generated motor current/ torque (motor torque $\propto$ motor current); third, continually variable speed, in essence (reference the Figure 1 which illustrates the torque–speed characteristics of electric motors); fourth, with small size and powerful output it can be easily located in-wheel motors (Marino *et al*., 2013; Ma *et al*., 2011; You *et al*., 2014).

Active control systems (such as ABS, 4WS and ESP, etc.) are widely used in traditional vehicles and is popular because they can cope with complex operating conditions and improve the security and comfort of vehicles (Kwon *et*

**Corresponding author.* e-mail: lkn@sjtu.edu.cn

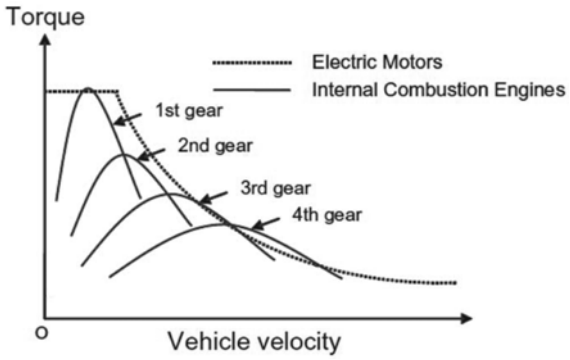

Figure 1. Torque-speed characteristics of electric motors and internal combustion engines.

al., 2015; Zhang *et al*., 2013b; Zheng *et al*., 2014). Typically, integrated vehicle dynamics control has attracted wide attention and has become a hot area of research in the domain (Song, 2012; Xiao *et al*., 2011; Gordon *et al*., 2003; Nagai *et al*., 2002; Yu *et al*., 2008; Vale *et al*., 2014; Li *et al*., 2008). Nonetheless, most studies focus on the calculation of tire friction or total yaw moment, rather than on its efficient implementation, though they do, in fact, enhance the performance of vehicles. Regardless of the tire friction generation mechanism, only some relatively simple methods (such as only allocating yaw moment to brake forces in one single axle (Gordon *et al*., 2003; Zhang *et al*., 2013b; Zheng *et al*., 2014; Ren *et al*., 2014) are being used currently. Due to the lack of consideration for the tire–road interaction, their strategy is possibly infeasible in practice. For example, when needing a lot of tire force, simply increasing brake force can make matters dangerous, especially if the slip ratio of the tire has been sufficiently large. There are some methods, such as nonlinear robust control, nonlinear optimum distribution, *et al.* (Yim, 2015; Hattori *et al*., 2002; Kim *et al*., 2014), which were used to fix this but the full realization of the tire friction problem indicates there is a urgent need for more research in this area, because it is the key issue to enhancing handling performance. Furthermore, the real-time tire-road friction force is the key factor for the AEBS, a subsystem of Advanced Driver Assistant System (ADAS) (Hassannejad *et al*., 2015), which can be used to estimate the Warning Index (WI) (Kusano and Gabler, 2012; Kim *et al*., 2015b; Lee *et al*., 2012).

In the past few years, due to the lack of proper sensors for internal combustion engine vehicles, precise value of tire-road friction forces is not available but a rough estimate has been made. However, the EVs can give a fine and accurate value. Because EVs use an in-wheel motor, the brake torque and angular acceleration of the wheel can be acquired easily.

A kind of main/servo loop integrated control structure has been presented previously, in several articles (Mokhiamar and Abe, 2004; Shen and Yu, 2004; Hou *et al*., 2015). The calculation of the desired stable forces of tires is the main part of the mail loop and the desired stable forces is produced in the servo loop. Previous articles have stated the main loop design and tire force contribution. In addition to the existing ABS, this paper is a comprehensive supplement added for EVs, and describes a way to parameters implement tire identification and control in servo loop.

The structure of this document is as follows: section II describes the tire model with in-wheel motor and the structure of Nov-ABS controller; section III calculates the expected longitudinal slip ratio; section IV implements that; section V uses the numerical simulation results to verify proposed method.

2. NOV-ABS AND CONTRLLER STRATEGY

In order to master the basic characteristics of braking system, this paper amends the problem of wheel slip-control due to only taking the longitudinal dynamics of the EV into account, while ignoring the effect of load transfer via a simplified dynamics model of a quarter-vehicle model with in-wheel motor which is shown in Figure 2, The dynamic equations of motion for this system please check the following description.

In this paper, we only consider the longitudinal dynamics of the vehicle. So, the problem of wheel slip control is best explained by looking at a quarter-car model as shown in Figure 3. The dynamic equations of motion of the system are

$$m\frac{du}{dt} = -F_{xb} \tag{1}$$

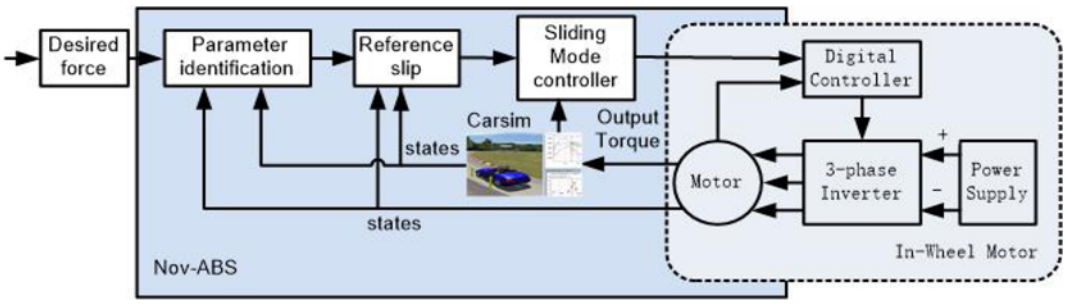

Figure 2. Control architecture of the Nov-ABS with In-wheel motor.

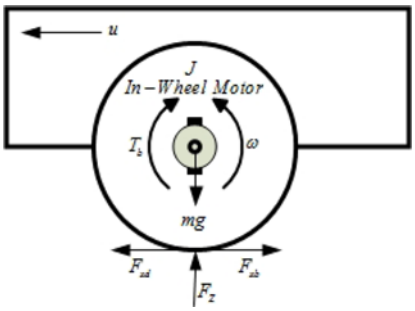

Figure 3. Quarter-car model.

$$J\frac{d\omega}{dt} = r_b F_{xb} - T_b \tag{2}$$

$$T_b = F_b r_b \tag{3}$$

$$F_Z = mg \tag{4}$$

Where:

m	is mass of quarter-car;
u	is horizontal velocity of vehicle movement;
F_{xb}	is friction between tire and road;
J	is the inertia of wheel;
ω	is wheel angular velocity;
r_b	is the radius of wheel;
T_b	is braking torque;
F_b	is braking force gained from in-wheel motor;
F_z	is vertical power;
g	is gravitational acceleration.

Note that u is estimated using the front and rear wheel center speed (Zhao *et al*., 2015) and F_b is get from T_b in-wheel motor, as shown in Figure 4.

In this study, a hysteresis-loop based current controller (Kazmierkowski and Malesani, 1998) is proposed and implemented to control the in-wheel motor, as illustrated in Figure 3. By tracking the error between measured current and reference current, the hysteresis-loop based current controller works as a current-loop controller for in-wheel motor via a three-phase inverter. In this way, the electromagnetic torque of the motor can follow the changing reference signal. For tire-road friction force is directly proportional to electromagnetic torque, which is expressed as:

$$F_b = \frac{\cot\varphi\cdot\eta_m}{r_b}\cdot T_m \tag{5}$$

And, electromagnetic torque T_m is proportional to current i which is expressed as:

$$T_m = 2\Phi\cdot i \tag{6}$$

The generated electromagnetic torque T_m is converted into braking force F_b by the in-wheel motor and mechanism, which can be expressed as:

$$F_b = \frac{T_b}{r_b} = \frac{\cot\varphi\cdot\eta_m}{r_b}\cdot T_m = \frac{2\cdot\Phi\cdot\cot\varphi\cdot\eta}{r_b}\cdot i \tag{7}$$

where φ is screw lead angle, Φ is the flux linkage, η_m, η is efficiency factor, i stands for the value of phase current.

In other words, the tire-road friction force can be computed by

$$\hat{F}_{xb} = \frac{J}{r_b}\frac{d\omega}{dt} + \frac{T_b}{r_b} = \frac{J}{r_b}\frac{d\omega}{dt} + \frac{2\cdot\Phi\cdot\cot\varphi\cdot\eta}{r_b}\cdot i \tag{8}$$

In terms of $\hat{F}_{xb}$, the longitudinal slip $\hat{\lambda}_{xb}$ can be computed by

$$\hat{\lambda}_{xb} = \frac{u-\omega r_b}{u} \tag{9}$$

Therefore, according to the real-time dynamic value of $\hat{F}_{xb}$, $\hat{\lambda}_{xb}$ and the reference tire model, the following equation can be acquired which means the Magic Formula will be adapted and the non-linear relationship of the tire-road friction force F_{xb} and the homologous λ_{xb} can be described by this equation

$$\frac{2\cdot\Phi\cdot\cot\varphi\cdot\eta}{r_b}\cdot i = F_{xb} = F_Z\cdot\mu_{xb}(\lambda_{xb}) \tag{10}$$

where μ_{xb} is the coefficient of friction

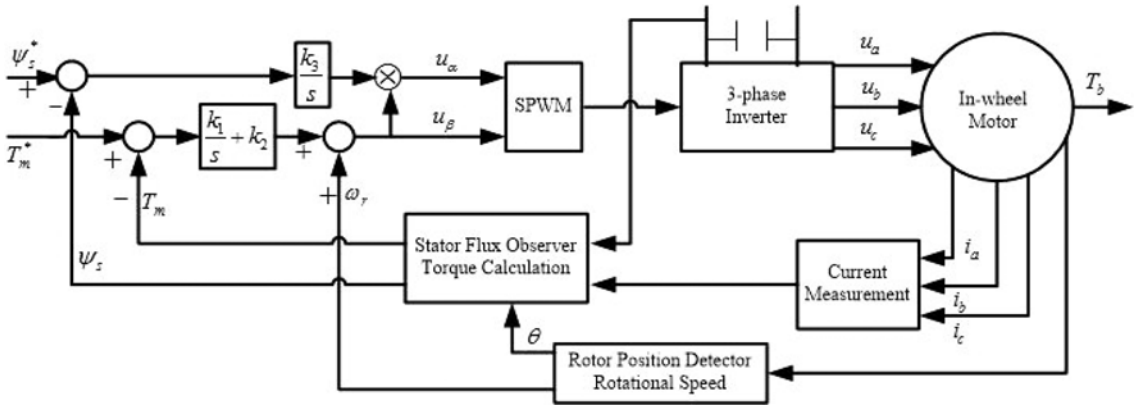

Figure 4. Control Block diagram of in-wheel motor.

In addition, because the control objective of Nov-ABS is to track any λ_{Ref} ($0<\lambda_{\mathrm{Ref}}\le\lambda_{\mathrm{Opt}}$) with respect to any craved forces and moments from the upper control layer, we can calculate the λ_{Ref} as regard to F_{Ref} (F_{Desired}) with numerical method of nonlinear equations according to the Equation (8). And finally we can get the following equation:

$$\begin{aligned}&F_{\mathrm{Ref}}-F_Z\cdot\mu^*_{\mathrm{Ref}}(\lambda_{\mathrm{Ref}})\\&=\frac{2\cdot\Phi\cdot\cot\varphi\cdot\eta}{r_{\mathrm{b}}}\cdot i_{\mathrm{Ref}}-F_Z\cdot\mu^*_{\mathrm{Ref}}(\lambda_{\mathrm{Ref}})=0\end{aligned}\tag{11}$$

3. CONSTRAINED SQP ALGORITHM FOR REFERENCE TIRE MODEL PARAMETERS IDENTIFICATION

The LuGre model is popular because its parameters have a physical significance and its velocity-dependency is also physically consistent. However, the quasi-static value of the aim slip is necessary for the controller design of ABS. So, the alleged Magic formula is the root of the reference tire model in this paper. In terms of research on vehicle dynamics, it is an extensively used semi-empirical tire model which be used to calculate steady-state tire force and moment characteristics. When given values of vertical load and the longitudinal dynamics of the vehicle, the general form of the formula can be expressed to the following equation.

$$\begin{aligned}&\mu_{\mathrm{L}}=\mu(\lambda,B_{\mathrm{L}},C_{\mathrm{L}},D_{\mathrm{L}},E_{\mathrm{L}})\\&=D_{\mathrm{L}}\sin[C_{\mathrm{L}}\arctan\{B_{\mathrm{L}}\lambda-E_{\mathrm{L}}(B_{\mathrm{L}}\lambda-\arctan(B_{\mathrm{L}}\lambda))\}]\end{aligned}\tag{12}$$

where μ_{L} the coefficient of longitudinal friction, λ the longitudinal slip, B_{L} stiffness factor, C_{L} shape factor, D_{L} peak value, E_{L} curvature factor.

In fact, the vehicle operating conditions are varied, for example, a wide variety of road conditions. Therefore, the Magic formula essential parameter (B_{L}, C_{L}, D_{L} and E_{L}) should be online estimated.

In order to bring the error between the estimated value and the true value of B_{L}, C_{L}, D_{L} and E_{L} to a minimum, a performance index is introduced in this paper. With the weighted sum of squares of the error of the estimated value and the true value $\hat{F}_{\mathrm{xb,i}}$ of the tire-road friction force, the original parameter recognition problem is transformed into a constrained optimization problem, and can be expressed to:

$$\begin{aligned}&\underbrace{\min}_{x}PI=\sum_{\mathrm{i}=1}^{\mathrm{N}}w_{\mathrm{i}}\left[\hat{F}_{\mathrm{xb,i}}-F_Z\mu(\hat{\lambda}_{\mathrm{xb,i}},x^{\mathrm{T}})\right]^2\\&x=\left[B_{\mathrm{L}},C_{\mathrm{L}},D_{\mathrm{L}},E_{\mathrm{L}}\right]^{\mathrm{T}}\end{aligned}\tag{13a}$$

$$s.t.\ \ x_{\min}\le x\le x_{\max}\tag{13b}$$

where

w_{i} weighting factor

The minimum and maximum constraint range for B_{L}, C_{L}, D_{L} and E_{L} respectively are $x_{\min}$ and $x_{\max}$.

With the implementation of the constrained SQP algorithm, we can propose a scheme to get the minimum value of *PI*. In this process, parameters are optimized by using the active-set Sequential Quadratic Programming (SQP) method, which is the most popular optimization algorithms and can reach the region near an optimum point relatively quickly with the boundary constraints.

Because the active set SQP approach is suitable for both the small inequality constrained problems and the large inequality constrained problems, it is considered to be the best choice for reference tire model parameters identification.

First, the upper and lower limits of the constraint Equation (13b) can be converted into conventional inequality constraints as follows

$$A_{\mathrm{c}}x\ge b_{\mathrm{c}}\tag{14}$$

$$A_{\mathrm{c}}=\left[I,-I\right]^{\mathrm{T}},b_{\mathrm{c}}=\left[x_{\min},-x_{\max}\right]^{\mathrm{T}}\tag{15}$$

where I is the 4 × 4 identity matrix.

Next, the definition of the Lagrangian for the constrained problem (10a) is following:

$$L(x,\varphi)=PI(x)-\sum_{\mathrm{i}\in\psi}\varphi_{\mathrm{i}}(\alpha_{\mathrm{i}}x-b_{\mathrm{i}})\tag{16}$$

where $i\in\psi$ is the inequality constraints. And in this part, the active set with any feasible x can be as expressed:

$$A_{\mathrm{a}}(x)=\{i\in\psi\mid A_{\mathrm{c}}x\ge b_{\mathrm{c}}\}\tag{17}$$

The optimization problem (11) can't be handled by Lagrangian methods because of the inequality-constraints straightly. Then, active set SQP methods are adopted here, which extend the inequality-constrained problem to equality-constrained one. In particular, each iteration $x^{(\mathrm{k})}$ will generate a subset of constraints which also are a called working set $I^{(\mathrm{k})}$ in this method and it only fixes equality-constrained sub-problems. Furthermore, in this process we just impose the constraints in the working sets as equalities and neglect all other constraints. Each iteration will update this working set following the rules which based on Lagrange multiplier estimates. Assuming that at the iteration $(x^{(\mathrm{k})},\varphi^{(\mathrm{k})})$ the quadratic programming is given as following:

$$\min\ q(p)=\nabla PI_{\mathrm{k}}^{\mathrm{T}}p+\frac{1}{2}p^{\mathrm{T}}W_{\mathrm{k}}p\tag{18a}$$

$$s.t.\quad A_{\mathrm{k}}^{\mathrm{T}}p+A_{\mathrm{c}}(x_{\mathrm{k}})-b_{\mathrm{c}}\ge 0\tag{18b}$$

At working set $I^{(\mathrm{k})}$, the equality-constraints optimization problem should be solved here

$$\begin{aligned}&\min\ \nabla PI_{\mathrm{k}}^{\mathrm{T}}p+\frac{1}{2}p^{\mathrm{T}}W_{\mathrm{k}}p\\&s.t.\quad a^{\mathrm{i}}p+A_{\mathrm{c}}^{\mathrm{i}}(x^{(\mathrm{k})})-b_{\mathrm{c}}^{\mathrm{i}}=0,i\in I^{(\mathrm{k})}\end{aligned}\tag{19}$$

Specifying $\delta = p - p^{(k)}$, we get

$$q(\delta + p^{(k)}) = \nabla PI_k^T \delta + \frac{1}{2}\delta^T W_k \delta + q(p^{(k)}) \tag{20}$$

Where $q(p^{(k)})$ and q are independent of each other. Because in the premise of not changing the problem solution, we can get $q(p^{(k)})$ from the objective, it can be expressed as follows that the QP sub-problem to be solved at the kth iteration

$$\min \ \nabla PI_k^T \delta + \frac{1}{2}\delta^T W_k \delta \tag{21a}$$

$$s.t. \quad a^i \delta = 0, i \in I^{(k)} \tag{21b}$$

Assume that the optimal δ_k selected from (21a) is not zero current, we need determine how long to move in this direction. For to the constraints, if $p_k + \delta_k$ is possible, $p_{k+1} = p_k + \delta_k$ be set, or else, $p_{k+1} = p_k + \alpha_k \delta_k$ be set.

In order to get the maximum reduction in q, we hope the subject is still feasible when α_k is as large as possible in [0, 1] range, then we get:

$$\alpha_k \overset{\text{def}}{=} \min\left(1, \min_{i \notin I^{(k)}, a^i \delta < 0} \frac{b_{c,i} - a_{c,i}^T p_k}{a_{c,i}^T \delta_k}\right) \tag{22}$$

In the quadratic model, all SQP method is dependent on a choice of W_k. When there is a way to approximate the Lagrangian Hessian, a quasi-Newton approximation must be used. For example, the BFGS updates formula by using Hessian approximation B_k instead of W_k, we set

$$\begin{aligned} s_k &= x_{k+1} - x_k \\ y_k &= \nabla_x L(x_{k+1}, x_{k+1}) - \nabla_x L(x_k, x_k) \end{aligned} \tag{23}$$

$$B_{k+1} = B_k - \frac{B_k s_k s_k^T B_k}{s_k^T B_k s_k} + \frac{y_k y_k^T}{s_k^T y_k} \tag{24}$$

But, this method will converge quickly when $\nabla_{xx}^2 L$ is positive-definite at the array of points x_k, on the contrary if it is negative, it doesn't work well by using the BFGS update.

The scheme which the update is definitely always well-defined the damped BFGS updating for SQP has been designed (Nocedal and Wright, 2006; Zhang *et al*., 2015). According to this scheme, the following equation is defined:

$$r_k = \theta_k y_k - (1 - \theta_k) B_k s_k \tag{25}$$

where the scalar θ_k is defined as

$$\theta_k = \begin{cases} 1, & if \ \ s_k^T y_k \geq 0.2 s_k^T B_k s_k \\ \dfrac{0.8 s_k^T B_k s_k}{s_k^T B_k s_k - s_k^T y_k}, & if \ \ s_k^T y_k < 0.2 s_k^T B_k s_k \end{cases} \tag{26}$$

Update B_k as follows

$$B_{k+1} = B_k - \frac{B_k s_k s_k^T B_k}{s_k^T B_k s_k} + \frac{r_k r_k^T}{s_k^T r_k} \tag{27}$$

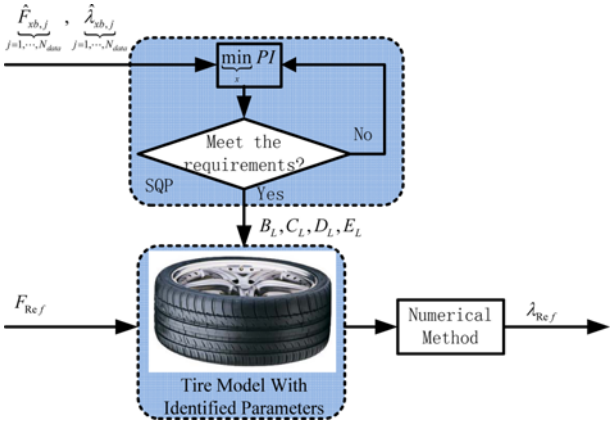

Figure 5. Flow chart of the calculation of desired longitudinal slip ratio.

It ensures that B_{k+1} is positive-definite.In accordance with the above description, the flow diagram of the constrained SQP algorithm is stated as follows:

And $\hat{F}_{xb}$ and $\hat{\lambda}_{xb}$ is defined by Equations (8) and (9).

4. SLIDING MODE CONTROLLER

Because this controller will be used in many uncertain conditions, such as a variety of road surface parameters and the noise from sensors, then it should be strong enough to adapt that. With regard to this reason, we introduce the sliding mode method in our paper to control this nonlinear system. At first, the definition of a time-varying sliding mode surface is given as follows:

$$s = \lambda - \lambda_{Ref} \tag{28}$$

The Equations (1), (2) and (6) will deduce the following equation:

$$\begin{aligned} \dot{\lambda} &= \frac{d\left(\dfrac{u - \omega r_b}{u}\right)}{dt} \\ &= \frac{\dfrac{-r_b^2 F_{xb}}{J} + (1 - \lambda)\dot{u}}{u} + \frac{2 \cdot \Phi \cdot \cot\varphi \cdot \eta \cdot i_b}{uJ} \end{aligned} \tag{29}$$

Setting

$$f_{mid} = \frac{\dfrac{-r_b^2 F_{xb}}{J} + (1 - \lambda)\dot{u}}{u} \tag{30}$$

has

$$\dot{\lambda} = f_{mid} + \frac{2 \cdot \Phi \cdot \cot\varphi \cdot \eta \cdot i_b}{uJ} \tag{31}$$

Because the tire slip λ is the only one parameters that may influence our estimates of the function f_{mid}, thus, we can draw the difference between the actual and the

predicted value of $\hat{f}_{\text{mid}}$ as follows:

$$e = f_{\text{mid}} - \hat{f}_{\text{mid}} = -\frac{\dot{u}}{u}(\lambda - \hat{\lambda}_{\text{Ref}}) \tag{32}$$

Hence, finding a positive function F_{mid} as following:

$$\left| f_{\text{mid}} - \hat{f}_{\text{mid}} \right| \le F_{\text{mid}} \tag{33}$$

The best approximation of a continuous control law will lead to $\dot{s} = 0$. Combined with the Equations (28), (30) and (31), we can get:

$$\dot{s} = f_{\text{mid}} + \frac{2 \cdot \Phi \cdot \cot\varphi \cdot \eta \cdot i_{\text{b}}}{uJ} - \dot{\lambda}_{\text{Ref}} = 0 \tag{34}$$

Then the estimation of T_{b} is

$$\hat{i}_{\text{b}} = -(f_{\text{mid}} - \dot{\lambda}_{\text{Ref}}) \frac{uJ}{2 \cdot \Phi \cdot \cot\varphi \cdot \eta} \tag{35}$$

We get the system track $\lambda - \lambda_{\text{Ref}} \equiv 0$ by defining the sliding surface $s = 0$, thus, we draw

$$i_{\text{b}} = \hat{i}_{\text{b}} - k_{\text{mid}}\, sgn(s) \tag{36}$$

To avoid dithering, where sign function $sgn(s)$ is replaced with the saturation function defined as

$$sat(s_{\text{i}}/\vartheta_{\text{i}}) = \begin{cases} sgn(s_{\text{i}}), & if \ \ |s_{\text{i}}| \ge \vartheta_{\text{i}} \\ s_{\text{i}}/\vartheta_{\text{i}} \ , & if \ \ |s_{\text{i}}| < \vartheta_{\text{i}} \end{cases}$$

Because $0 \le \left| \lambda - \hat{\lambda}_{\text{Ref}} \right| \le 1$

letting $F_{\text{mid}} = \left| -\frac{\dot{u}}{u} \right|$ from Equation (32)

and

$$k_{\text{mid}} = (F_{\text{mid}} + \eta) \cdot \frac{uJ}{2 \cdot \Phi \cdot \cot\varphi \cdot \eta \cdot r_{\text{b}}},$$

we get:

$$\begin{aligned} \frac{1}{2}\frac{ds^2}{dt} &= s\dot{s} = s(\dot{\lambda} - \dot{\lambda}_{\text{Ref}}) \\ &= \text{s}\left[\begin{array}{l} \left(f_{\text{mid}} + \dfrac{2 \cdot \Phi \cdot \cot\varphi \cdot \eta \cdot i_{\text{b}}}{uJ} \right) \\ -\left(\hat{f}_{\text{mid}} + \dfrac{2 \cdot \Phi \cdot \cot\varphi \cdot \eta \cdot \hat{i}_{\text{b}}}{uJ} \right) \end{array} \right] \\ &= \text{s}\left[(f_{\text{mid}} - \hat{f}_{\text{mid}}) + \frac{i_{\text{b}} - \hat{i}_{\text{b}}}{uJ} \right] \\ &\le \text{s}\left[\begin{array}{l} F_{\text{mid}} - \dfrac{2 \cdot \Phi \cdot \cot\varphi \cdot \eta \cdot r_{\text{b}}}{uJ} \cdot \\ (F_{\text{mid}} + \eta) \cdot \dfrac{uJ}{2 \cdot \Phi \cdot \cot\varphi \cdot \eta \cdot r_{\text{b}}} sign(s) \end{array} \right] \\ &= \text{s}\left[\eta\, sign(s) \right] \le -\eta |s| \end{aligned} \tag{37}$$

The sliding condition is fulfilled because η is a positive constant. This means that the sliding surface defined above can be realized through the designed control law.

5. SIMULATIONS RESULTS AND ANALYSIS

In order to verify the validity of the proposed controllers, we conducted a co-simulation with Carsim, Matlab/Simulink and the simulation bench from this part (Ma *et al*., 2011). The controller of Nov_ABS is designed using Matlab/Simulink and the vehicle model is proposed using the Carsim, which is used worldwide by over 110 OEMs and Tier 1 suppliers and over 200 universities and government research labs. And the simulation bench, as shown in Figure 6, is used as the validation tool which is the test bench of the HIL for the next work. For the reason that the wheel dynamic is very fast dynamics, the sampling time of simulation for parameters identification is 10 ms and 100 ms for the controller of ABS, which should be work more than 10 times per sec.

To start with, a torsional system is applied to our test platform. Please reference the Figure 6. In this torsional system, a long torsional shaft is used to connect the drive side and the load side of the flywheels; meanwhile, gears transmit the drive torque from the drive servomotor to the axis by the gear ratio 1 : 2. The load servomotor is used as the dynamometer in this lab. ± 3.84 Nm is the largest

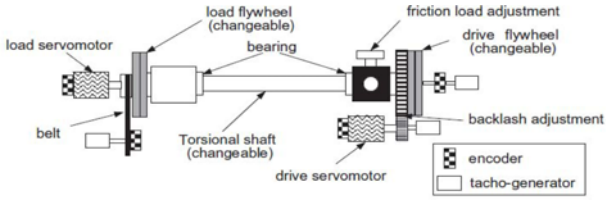

Figure 6. Simulation bench.

Table 1. Parameters on different road surface.

Notation	Value	Unit
m mass of quarter-car	372.5	kg
u vehicle velocity	100	km/h
g acceleration of gravity	9.8	m/s^2
J wheel inertia	16	kg·m^2
r_{b} wheel radius	0.28	m
$B_{\text{L,min}}$ lower bond of stiffness factor	8	-
$C_{\text{L,min}}$ lower bond of shape factor	1	-
$D_{\text{L,min}}$ lower bond of peak value	0.1	-
$E_{\text{L,min}}$ lower bond of curvature factor	0.1	-
$B_{\text{L,max}}$ upper bond of stiffness factor	18	-
$C_{\text{L,max}}$ upper bond of shape factor	1.7	-
$D_{\text{L,max}}$ upper bond of peak value	1.5	-
$E_{\text{L,max}}$ upper bond of curvature factor	0.9	-

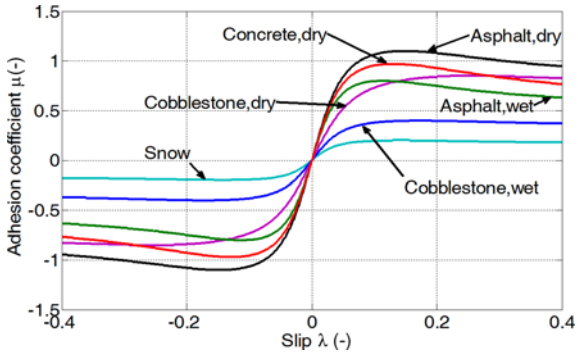

Figure 7. μ-λ curve of different road surface.

Table 2. Parameters used in simulations.

Road	B_L	C_L	D_L	E_L
Snow	17.430	1.4500	0.20	0.6500
Cobblestone, wet	14.027	1.4500	0.40	0.6000
Asphalt, wet	15.635	1.6000	0.80	0.4500
Cobblestone, dry	10.695	1.4000	0.85	0.6450
Concrete, dry	13.427	1.6402	0.97	0.5372
Asphalt, dry	13.427	1.5500	1.10	0.5327

output torque of the two brushless DC servomotors. An optical encoder is used to detect the angular position and the speed of the two motors and this optical encoder must be with a resolution of 8000 pulses per revolution.

Table 1 gives some Magic Formula's empirical parameters on different road surfaces and Figure 7 gives these roads' μ-λ curves.

Based on the previous description, the constrained range of B_L, C_L, D_L and E_L can be acquired correspondingly. In addition, the Table 2 shows the parameters chosen in this simulations lab (Li *et al*., 2012).

In next section, we have implemented the simulations in wide variety of circumstances to better validate the effectiveness of our proposed identification scheme.

Figures 8 ~ 11 give the identification results. Different range of sampling points $\hat{F}_{xb}$ and $\hat{\lambda}_{xb}$ is a part of the diversification of the test environment, which is from the experimental data using at the test platform as shown in Figure 5. Besides, the true value of B_L, C_L, D_L and E_L is used to draw the true value of μ and the identified value of B_L, C_L, D_L and E_L is used to draw the identified value of μ.

The identified value of μ will be within the scope of $\lambda \in [0, 0.08]$ when $\hat{\lambda}_{xb,j}(j = 1, 2, \cdots, N_{data})$ in the scope of [0, 0.01], as illustrated in Figure 8. According to Figure 9, we can get that the value of 0.02 is the maximum for the error between true and identified value of μ. When the scope of sampling points $\hat{\lambda}_{xb,j}(j = 1, 2, \cdots, N_{data})$ is changed from $[0, 0.01]$ to $[0.125, 0.135]$, which is shown in Figure 10, the identification result of that important points also has the

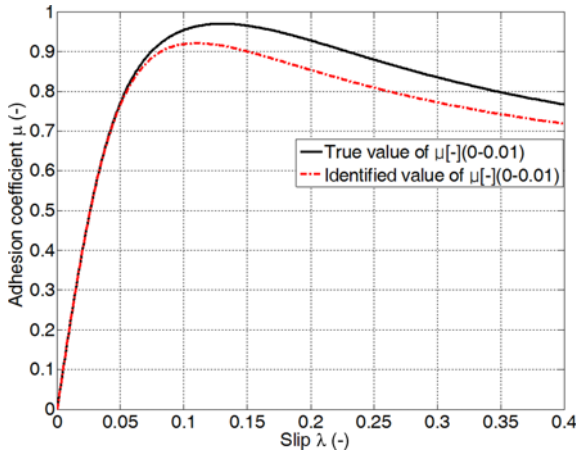

Figure 8. True and identified value of μ ($\lambda \in [0, 0.01]$).

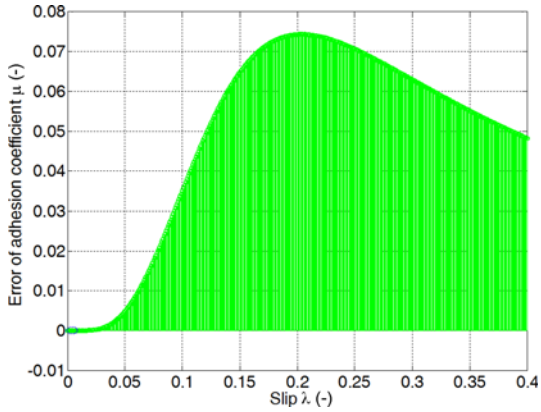

Figure 9. Error of true and identified value of μ ($\lambda \in [0, 0.01]$).

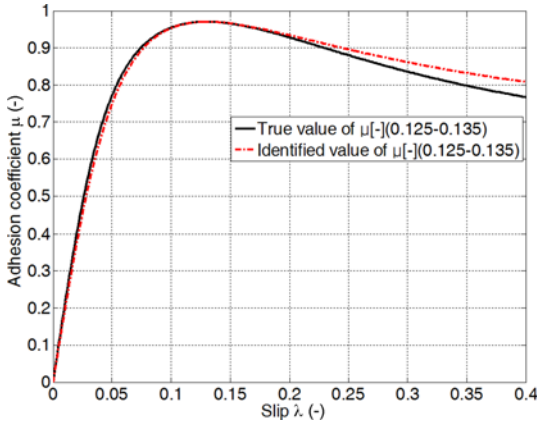

Figure 10. True and identified value of μ ($\lambda \in [0.125, 0.135]$).

remarkable enhancement and these important points contain a lot of useful information of the non-linear characteristics of tire-road friction. From Figures 10 and 11, we can obtain that the value of 0.02 is the maximum for the deviation of true and identified value of μ in the scope

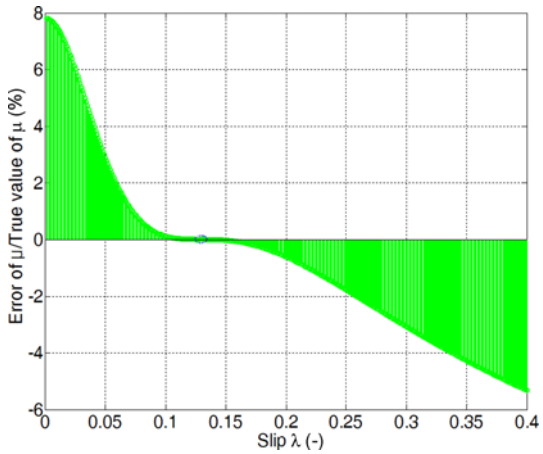

Figure 11. Error of true and identified value of μ ($\lambda \in [0.125, 0.135]$).

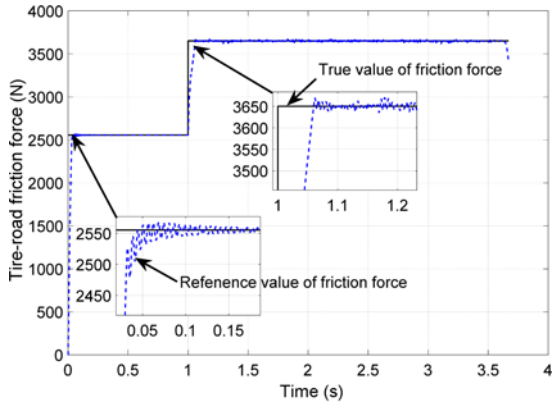

Figure 12. Reference and true value of friction force (Same road, different F_{Ref}).

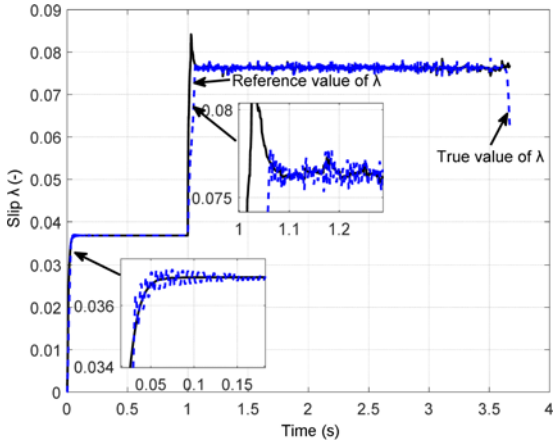

Figure 13. Reference and true value of λ (Same road, different F_{Ref}).

of $\lambda \in [0.06, 0.25]$. What's more, as shown in Figure 11, when the range is $\lambda \in [0, 0.4]$ the maximum deviation is close to 0.03 and this deviation percentage is less than 5 %.

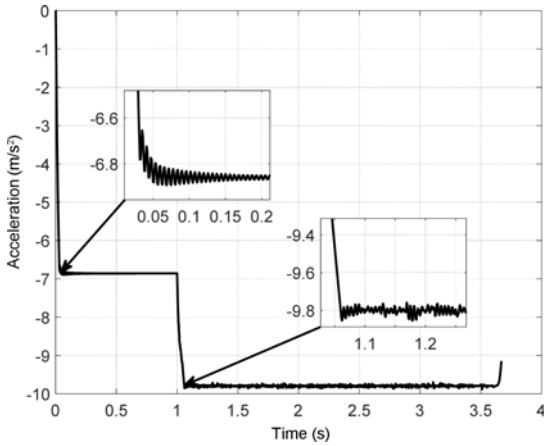

Figure 14. Vehicle acceleration (Same road, different F_{Ref}).

In summary, the identification results are consistent with our expectations in these ranges according to the above experimental data and analysis.

At last, the lower-level controller design is the core of our work in this article. Here, we simulate the braking process to access the performance of the Nov-ABS. We give the simulation results for three cases (Case A, B and C), as shown in Figures 12 ~ 19:

Case A: The vehicle is exposed to a constant reference friction force F_{Ref}, with setting the input to 2555.4N at 0 second and the input to 3651 at 1.0 second on the same road with asphalt, dry surface. Found at the Figures 12 ~ 15, which demonstrated the vehicles dynamic response.

After a period of time delay, shown in Figure 12, the estimated friction force is almost consistent with the reference value F_{Ref}. The estimated value and the tracking results of λ_{Ref} regarding F_{Ref} are given in Figure 13. Figure 13 gives the different value of F_{Ref} corresponding to the different value of λ_{Ref} with the same road condition. It is well known that the Nov_ABS can evaluate and explore λ_{Ref}. The absolute value of vehicle acceleration rises from

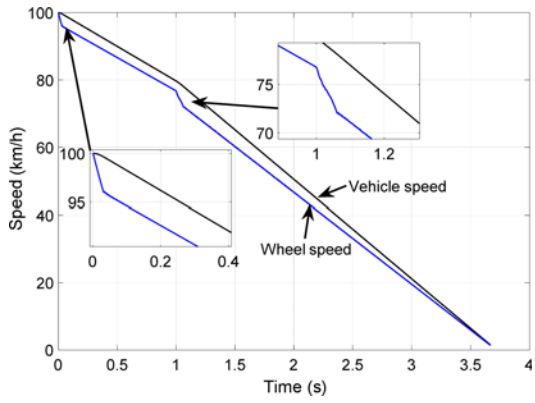

Figure 15. Vehicle and wheel speed (Same road, different F_{Ref}).

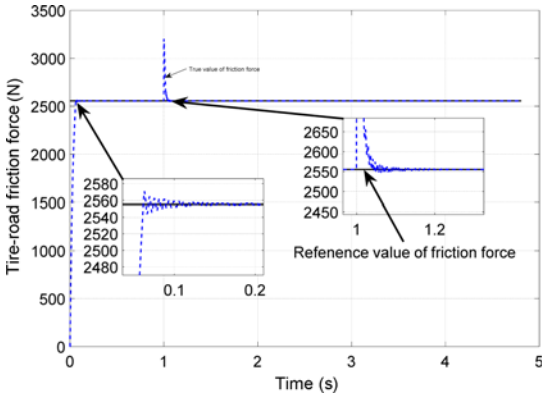

Figure 16. Reference and true value of friction force (Different road, same F_{Ref}).

about 6.68 km/s^2 to 9.5925 km/s^2 along with the F_{Ref} changes, as indicated in Figure 14. Figure 15 presents the simulation result of the wheel and vehicle speed and we can get that the speed of wheel and vehicle goes with the changes of λ_{Ref}. Based on above description, although maybe the tracking result is not perfect, but at least it is good.

Case B: The vehicle is exposed to a constant reference friction force F_{Ref}, with setting the input to 2555.4N during the braking process. Figures 16 ~ 19 give the simulation results when the road conditions change from wet asphalt to dry asphalt at the second 1.0.

With the same F_{Ref}, according to Figures 16 and 18, we can conclude that there is a little change in the whole process about the true value of friction force and vehicle acceleration. Figure 19 also proven this conclusion. What's more, let us focus on the Figure 16, when the road conditions changes, we can get that there is a reduction about the reference value of λ_{Ref} and the value decreased from about 0.05545 to 0.03697 at 1.0 second although F_{Ref} invariable. With the results of simulation experiment, we can get that the tracking value of λ_{Ref} and the reference λ_{Ref} are consistent, which is in line with our desired effect.

Case C: The vehicle is exposed to a continuous changing reference friction force F_{Ref}, shown in Figure 20.

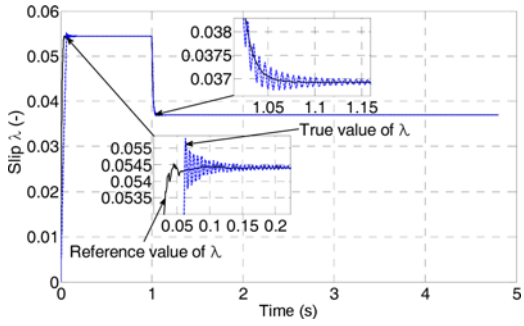

Figure 17. Reference and true value of λ (Different road, same F_{Ref}).

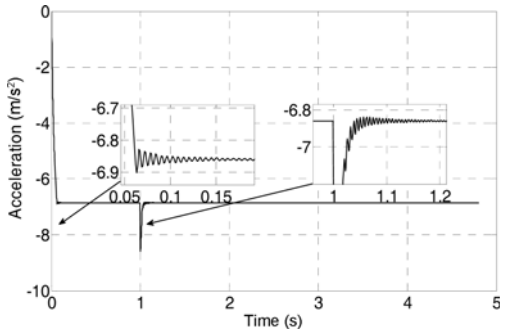

Figure 18. Vehicle acceleration (Different road, same F_{Ref}).

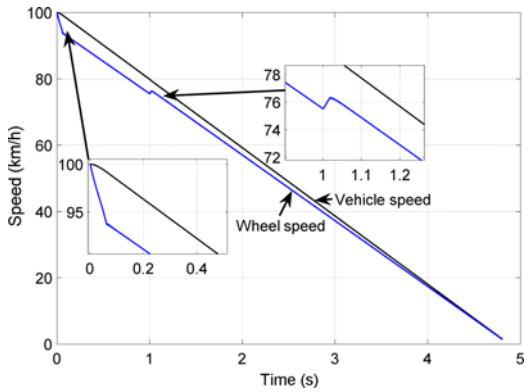

Figure 19. Vehicle and wheel speed (Different road, same F_{Ref}).

The simulation results are shown in Figures 20 ~ 23.

With changing F_{Ref}, according to Figures 20 and 22, we can conclude that there is a continuous change in the whole process about the true value of friction force and vehicle acceleration. Figure 23 also proves this conclusion. What's more, let us focus on the Figure 21, when the road conditions changes, we can get that there is a reduction about the reference value of λ_{Ref} and the value increased from about 0 to 0.03697 at 0.5 second and from 1.67 second to 5 second, the λ_{Ref} changed according to the

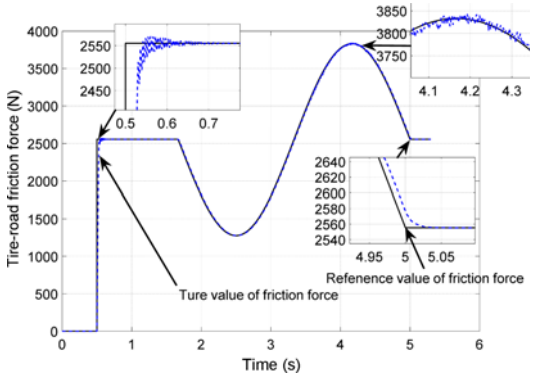

Figure 20. Reference and true value of friction force (Same road, different F_{Ref}).

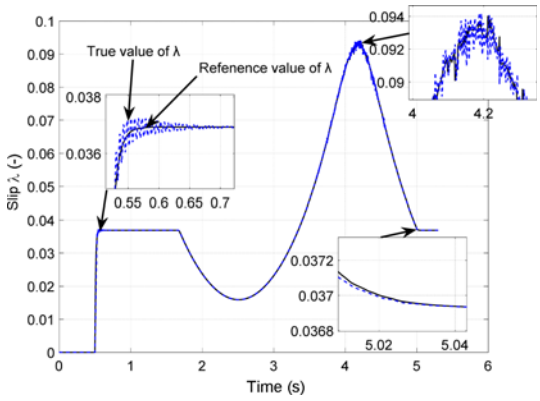

Figure 21. Reference and true value of λ (Same road, different F_{Ref}).

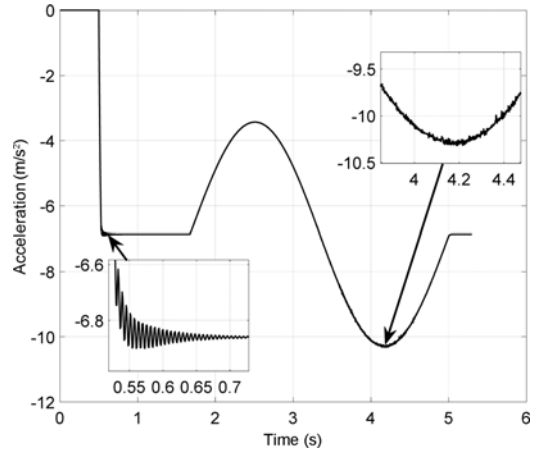

Figure 22. Vehicle acceleration (Same road, different F_{Ref}).

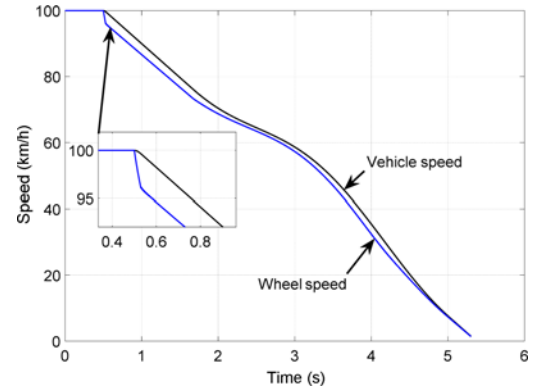

Figure 23. Vehicle and wheel speed (Same road, different F_{Ref}).

sinusoidal changing F_{Ref}. With the results of simulation experiment, we can get that the tracking value of λ_{Ref} and the reference λ_{Ref} are consistent, which is in line with our desired effect.

As described in Case A, Case B and Case C, with changing road surface, the proposed control strategy is still an acceptable adaptation. The proposed control strategy can provide an agreeable adaptation to the variable condition of road surface according to the results of Case A, Case B and Case C.

6. CONCLUSION AND FUTURE WORK

Vehicle integrated control is an active area of research, and our main/servo loop control strategy is its typical case. The key point of this work is a component of the servo loop which using in-wheel motor at Nov_ABS to achieve tire friction control self-adapting to the road surface as conditions change, which is targeted not only to estimate and track any tire-road friction force, but the maximum tire-road friction force, based on ABS. We proposed a two-step solution: the first step is online recognition of Magic Formula parameters with SQP method and acquirement of Nov_ABS objective with numerical method accordingly; the second step is dynamic implementation of Nov_ABS by using a nonlinear sliding mode control method.

The research is dedicated to the study of distributed micro-electric vehicles with in-wheel motors having comprehensively integrated control. This work includes the integration of the proposed Nov_ABS and the main loop controller and also the introduction of optimal & robust control to the main loop to seize parameter incertitude.

ACKNOWLEDGEMENT–This work was partially supported by the Science and Technology Planning Project of Guangdong Province under Grant No. 2014B010118002, and the National Natural Science Foundation of China under Grant No. 51375298 and No. 51208500. The first author would like to express appreciation to Dr. Kening Li and Pro. Fan Yu for valuable discussions that improved the quality and presentation of the paper.

REFERENCES

Attia, R., Orjuela, R. and Basset, M. (2014). Combined longitudinal and lateral control for automated vehicle guidance. *Vehicle System Dynamics* **52**, **2**, 261–279.

Gordon, T., Howell, M. and Brandao, F. (2003). Integrated control methodologies for road vehicles. *Vehicle System Dynamics* **40**, **1-3**, 157–190.

Hassannejad, H., Medici, P., Cardarelli, E. and Cerri, P. (2015). Detection of moving objects in roundabouts based on a monocular system. *Expert Systems with Applications* **42**, **9**, 4167–4176.

Hattori, Y., Koibuchi, H. and Yokayama, T. (2002). Force and moment control with nonlinear optimum distribution for vehicle dynamics. *6th Int. Symp. Advanced Vehicle Control (AVEC'02)*, Hiroshima, Japan.

Hori, Y. (2004). Future vehicle driven by electricity and control-research on four-wheel-motored 'UOT Electric March II'. *IEEE Trans. Industrial Electronics* **51**, **5**, 954–962.

Hou, Y., Edara, P. and Sun, C. (2015). Situation assessment and decision making for lane change assistance using ensemble learning methods. *Expert Systems with Applications* **42**, **8**, 3875–3882.

Kazmierkowski, M. P. and Malesani, L. (1998). Current control techniques for three-phase voltage-source PWM converters: A survey. *IEEE Trans. Industrial Electronics* **45**, **5**, 691–703.

Kim, S. and Huh, K. (2016). Fault-tolerant braking control with integerated EMBs and regenerative in-wheel motors. *Int. J. Automotive Technology* **17**, **5**, 923–936.

Kim, S. J., Kim, K.-S. and Yoon, Y.-S. (2015a). Development of a tire model based on an analysis of tire strain obtained by an intelligent tire system. *Int. J. Automotive Technology* **16**, **5**, 865–875.

Kim, S., Oh, H., Suk, J. and Tsourdos, A. (2014). Coordinated trajectory planning for efficient communication relay using multiple UAVs. *Control Engineering Practice*, **29**, 42–49.

Kim, T., Lee, J. and Yi, K. (2015b). Enhanced maximum tire-road friction coefficient estimation based advanced emergency braking algorithm. *Intelligent Vehicles Symp., IEEE*.

Kusano, K. D. and Gabler, H. C. (2012). Safety benefits of forward collision warning, brake assist, and autonomous braking systems in rear-end collisions. *IEEE Trans. Intelligent Transportation Systems* **13**, **4**, 1546–1555.

Kwon, M. H., Park, J. H., Gwak, G. S., Huh, J. W., Choi, H. K. and Hwang, S. H. (2015). Cooperative control for friction and regenerative braking systems considering dynamic characteristic and temperature condition. *Int. J. Automotive Technology* **17**, **3**, 437–446.

Lee, D., Kim, B., Yi, K. and Lee, J. (2012). Development of an integrated driving path estimation algorithm for ACC and AEBS. *Spring Conf. Proc., Korean Society of Automotive Engineers*, 1030–1036.

Li, D., Du, S. and Yu, F. (2008). Integrated vehicle chassis control based on direct yaw moment, active steering and active stabiliser. *Vehicle System Dynamics* **46**, **S1**, 341–351.

Li, K., Cao, J. and Yu, F. (2012). Adaptive longitudinal friction control based on nonsingular and fast terminal sliding mode method. *WSEAS Trans. Systems* **11**, **8**, 409–418.

Ma, C., Xu, M. and Wang, H. (2011). Dynamic emulation of road/tyre longitudinal interaction for developing electric vehicle control systems. *Vehicle System Dynamics* **49**, **3**, 433–447.

Marino, R., Scalzi, S., Tomei, P. and Verrelli, C. M. (2013). Fault-tolerant cruise control of electric vehicles with induction motors. *Control Engineering Practice* **21**, **6**, 860–869.

Mokhiamar, O. and Abe, M. (2004). Simultaneous optimal distribution of lateral and longitudinal tire forces for the model following control. *J. Dynamic Systems Measurement & Control* **126**, **4**, 753–763.

Nagai, M., Shino, M. and Gao, F. (2002). Study on integrated control of active front steer angle and direct yaw moment. *JSAE Review* **23**, **3**, 309–315.

Nocedal, J. and Wright, S. J. (2006). *Numerical Optimization*. 2nd edn. Springer. New York, USA, 467–540.

Ren, D. B., Zhang, G. Z. and Wang, C. (2014). Adaptive method to trajectory tracking for lane changing. *Applied Mechanics and Materials*, **590**, 413–417.

Shen, X. and Yu, F. (2004). Study on vehicle chassis control integration based on a main-loop-inner-loop design approach. *Proc. Institution of Mechanical Engineers, Part D: J. Automobile Engineering* **220**, **11**, 1491–1502.

Song, J. (2012). Integrated control of brake pressure and rear-wheel steering to improve lateral stability with fuzzy logic. *Int. J. Automotive Technology* **13**, **4**, 563–570.

Vale, A., Fonte, D., Valente, F. and Ribeiro, I. (2014). Trajectory optimization for autonomous mobile robots in ITER. *Robotics and Autonomous Systems* **62**, **6**, 871–888.

Xiao, H., Chen, W., Zhou, H. and Zu, J. W. (2011). Integrated control of active suspension system and electronic stability programme using hierarchical control strategy: Theory and experiment. *Vehicle System Dynamics* **49**, **1**, 381–397.

Yim, S. J. (2015). Unified chassis control with electronic stability control and active front steering for under-steer prevention. *Int. J. Automotive Technology* **16**, **5**, 775–782.

You, F., Zhang, R. H., Wang, H. W., Xu, J. M. and Wen, H. Y. (2014). Dynamic model and tracking control of tractor semi-trailer vehicle with underactuated system. *J. Jilin University Engineering and Technology Edition* **44**, **5**, 1296–1302.

Yu, F., Li, D. F. and Crolla, D. A. (2008). Integrated vehicle dynamics control –state-of-the art review. *Vehicle Power and Propulsion Conf.*, 1–6.

Zhang, R., Ge, P., Zhou, X. and Wang, R. (2013b). An method for vehicle-flow detection and tracking in real-time based on gaussian mixture distribution. *Advances in Mechanical Engineering*, **5**, 861321.

Zhang, W., Liu, J., Cho, C. and Han, X. (2015). A hybrid parameter identification method based on bayesian approach and interval analysis for uncertain structures. *Mechanical Systems and Signal Processing*, **60-61**, 853–865.

Zhang, Z., Chau, K. T. and Wang, Z. (2013a). Analysis and stabilization of chaos in the electric-vehicle steering system. *IEEE Trans. Vehicular Technology* **62**, **1**, 118–126.

Zhao, Z., Yang, J. and Wu, X. (2015). Vehicle speed estimation based on distributed Kalman filter for four wheel drive hybrid electric car. *J. Mechanical Engineering* **51**, **16**, 50–56.

Zheng, J., Suzuki, K. and Fujita, M. (2014). Predicting driver's lane-changing decisions using a neural network model. *Simulation Modelling Practice and Theory*, **42**, 73–83.